Reorientational motion and Li^+-ion transport in $Li_2B_{12}H_{12}$ system: Molecular dynamics study

Kartik Sau,[1,*] Tamio Ikeshoji,[1,2] Sangryun Kim,[2] Shigeyuki Takagi,[2] Kazuto Akagi,[3] and Shin-ichi Orimo[2,3]

[1]*Mathematics for Advanced Materials - Open Innovation Laboratory (MathAM-OIL), National Institute of Advanced Industrial Science and Technology (AIST), c/o Advanced Institute of Material Research (AIMR), Tohoku University, Sendai 980-8577, Japan*

[2]*Institute for Materials Research (IMR), Tohoku University, Sendai 980-8577, Japan*

[3]*Advanced Institute for Materials Research (AIMR), Tohoku University, Sendai 980-8577, Japan*

(Received 25 March 2019; published 15 July 2019)

$Li_2B_{12}H_{12}$ and its derivatives are promising solid electrolytes for solid-state batteries. In this work, a potential model is proposed, and an extensive classical molecular dynamics study is performed to understand the origin of the fast ion conduction in $Li_2B_{12}H_{12}$. The proposed potential model reveals structural and dynamical properties of $Li_2B_{12}H_{12}$ that are consistent with first-principles molecular dynamics simulation and experimental results. The mechanism of Li^+-ion transport is studied systematically. The low-temperature α phase exhibits negligible diffusivity within a timescale of a few nanoseconds, whereas the high-temperature β phase with a similar crystal structure and larger lattice parameter exhibits entropy-driven high Li^+-ion diffusion assisted by anionic reorientation. We explicitly demonstrate the role of closo-borane anionic reorientational motion in the Li^+-ion diffusion and explain how the cell parameter facilitates the anionic reorientational motion. In addition, enhancing the degree of H freedom (by changing the B-B-H angular force parameters) results in significantly high cationic diffusivity at low temperature. Further insight into Li^+-ion transport is obtained by constructing a three-dimensional density map and determining the free-energy barrier, and the factors affecting cationic diffusion are thoroughly investigated with high precision using long simulations (5 ns).

DOI: 10.1103/PhysRevMaterials.3.075402

I. INTRODUCTION

Rechargeable lithium-ion batteries have played a major role in the past few decades as power devices for electric vehicles and stationary energy storage. In this context, solid-state batteries (SSBs), for which both the electrodes and electrolyte are solid, have received considerable attention because of their high energy density, long life span, and nonexplosive and nonvolatile nature [1–4]. However, their low ionic conductivity compared with liquid or polymer ionic conductors has presented a major issue. Recently, numerous solid fast ion conductors have been synthesized that exhibit conductivity comparable to that of liquid or polymer ionic conductors. Some recently discovered solid fast ion conductors include $Li_{10}GeP_2S_{12}$ [5], Li_3PS_4 [6], garnet-type $Li_7La_3Zr_2O_{12}$ [7–9], sodium superionic conductors [10,11], and hydride electrolytes [12].

Among the various materials reported to date, complex borohydrides are considered outstanding potential candidates for the solid electrolyte in SSBs because of the high Li- or Na-ion conductivity (exceeding 10^{-1} S cm^{-1}) [12–20], which enables a wide range of chemical substitutions and opens up the possibility of searching for even better ion-conductive materials. The general form of metal borohydrides is written as $M_x(M'_yH_z)$, where M can be replaced by alkali or alkaline-earth atoms. Typical complex M'_yH_z anions include BH_4^- [21,22], $B_6H_6^{2-}$, $B_{10}H_{10}^{2-}$, $CB_9H_{10}^-$, $B_{12}H_{12}^{2-}$, and $CB_{11}H_{12}^-$ [19]. Among the cations, lithium-ion electrolytes are a key component of all SSBs. Our major focus in this study is on $Li_2B_{12}H_{12}$, a starting member in this series, because of its superior stability against lithium metal and its high ionic conductivity. The low-temperature and low-conducting phase is the α phase, and the high-conducting and high-temperature phase is the β phase (Fig. 1) [23]. The high ionic conductivity is achieved mainly through the reorientational motion of the large cagelike $B_{12}H_{12}^{2-}$ anions located at face-centered cubic (fcc) positions, with the Li^+ ions occupying the interstitial sites of the anions. Although the $B_{12}H_{12}^{2-}$ units are isolated and fairly high reorientational motion is detected in the high-conducting phase, the $B_{12}H_{12}^{2-}$ is still stable in their positions [24].

According to recent studies on $Li_2B_{12}H_{12}$, several factors contribute to the fast ion transport. One major focus has been on understanding how the anionic reorientational motion is responsible for the cationic movement [25]. The reported reorientational motion of anion in the literature could possibly play a role in generating Li-site vacancies at the high-conducting phase, which will be investigated in this paper. The optimal Li-ion vacancy in the system generally enhances configurational entropy that might be a direction to maximize the ionic conduction, as observed in various other materials (Li_3PS_4 [6], and $Na_{1+x}Zr_2Si_xP_{3-x}O_{12}$ [26]). Therefore, more microscopic insight into the anionic motion, cationic path migration, and microscopic energy barriers of

*kartik.sau@gmail.com

Published by the American Physical Society under the terms of the Creative Commons Attribution 4.0 International license. Further distribution of this work must maintain attribution to the author(s) and the published article's title, journal citation, and DOI.

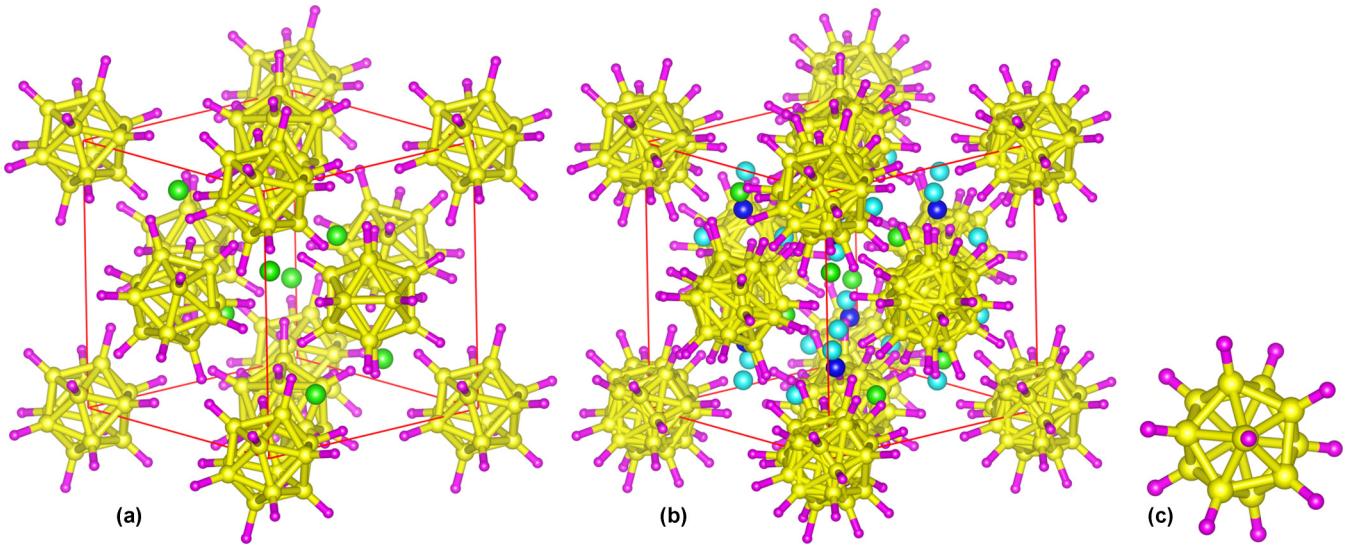

FIG. 1. Ball-and-stick model of $Li_2B_{12}H_{12}$. (a) Low-temperature α phase (the occupancy of Li, B, and H at each site is 1.0). (b) High-temperature β phase (the occupancy of both B and H is 0.5) [23]. (c) $B_{12}H_{12}^{2-}$ icosahedral unit with full occupancy. The yellow and pink balls represent B and H, respectively. The green, cyan, and blue colors represent the 8*c*, 24*d*, and tetragonal Li sites, respectively. The $B_{12}H_{12}^{2-}$ units are located in the fcc position, and the unit cell is marked by the red line.

ion hopping is needed. It is difficult to gain such an atomistic label of understanding simply by using experimental probes. Molecular dynamics (MD) simulation provides a potential alternative [27,28]. A set of first-principles MD (FPMD) simulations was recently performed on this material, $Li_2B_{12}H_{12}$ [18], to understand the factors affecting the cationic diffusion. However, the current understanding of the cationic diffusion assisted by anionic reorientational motion is limited because FPMD is limited to several tens of picoseconds because of the computational expense. It is difficult to understand the reorientational mechanism using FPMD as it typically occurs in a few hundred picoseconds. Although classical MD (CMD) is sensitive to the pair potential, simulations can reach up to few microseconds and can address larger systems. In addition, CMD allows several virtual experiments to be performed (which might not be possible in experiments or using FPMD), which can provide an explicit understanding of the factors responsible for the ion-hopping mechanism with tuning of different potential parameters. These benefits of CMD are applicable to other materials in this series ($MCB_{11}H_{12}$, $M_2B_{10}H_{10}$, where M = Li, Na, etc.) with slight modification if the potential model can be transferred. In this context, modeling the potential parameter to perform CMD would play a major role in opening up various theoretical studies to understand fundamentals of ion-hopping mechanisms. The potential of CMD has already been proven in systems such as AgI [29], beta-alumina [30], $Na_2M_2TeO_6$ (M = Ni^{2+}, Zn^{2+}, Co^{2+}, or Mg^{2+}) [31–34], $Na_{1+x}Zr_2Si_xP_{3-x}O_{12}$ [26], and some liquids [35], where it satisfactorily mimicked various experimental observations.

In this paper, we will develop interatomic potential parameters that satisfactorily reproduce vibrational spectra, structure, and diffusion coefficients in Secs. III A and III B. The long-time behavior of anionic reorientation will be described in Sec. III B. In Sec. III C, we will describe the ion-transport mechanism (with van Hove correlation function and cationic density profiles), and the influencing factors responsible for cationic diffusion will be investigated in Sec. III D.

II. METHODOLOGY

Force-field-based isothermal molecular dynamics (NVT-MD) simulations were performed at 600 K for the α and β phases employing the Coulomb-Buckingham and harmonic-type interatomic potential $U(r)$ [29,36–40],

$$U(r) = \frac{q_i q_j}{r} + A\exp(-r/\rho) - \frac{C}{r^6},$$
$$U(r) = \frac{1}{2}k_r(r - r_0)^2, \quad (1)$$
$$U(\theta) = \frac{1}{2}k_\theta(\theta - \theta_0)^2,$$

where r is the interatomic distance; q_i is the charge of the ith ion; A and ρ are the strength and range of overlapping repulsion, respectively; C is the van der Waals interaction between the pair of ions; k_r and k_θ are the spring constants of the bond and angle, respectively; and r_0 and θ_0 are the equilibrium bond and angle, respectively. The values of these parameters are listed in Table I. Given the high Coulombic charge of $B_{12}H_{12}^{2-}$ anions, the anion-anion repulsion is significantly high, which does not stabilize the structure. Hence, an attractive part is necessary, and we incorporated van der Waal interaction within interboron pairs. The parameters were obtained by empirical fitting of the structure, vibrational frequencies, and cation-hopping barrier from FPMD.

The NVT-MD simulation was performed by employing the software package lammps [41]. A unit cell contains four formula units of $Li_2B_{12}H_{12}$, whereas the simulated supercell consisted of $2 \times 2 \times 2$ cubic ($Pa\bar{3}$) unit cells of $Li_2B_{12}H_{12}$ containing a total of 832 atoms (64 Li, 384 B, and 384 O) with cell parameters a = 9.577 Å (α phase) [42] and 10.02 Å

TABLE I. Determined interionic pair potential parameters employed in this study.

x	q_x (e)	$A_{x\mathrm{Li}}$ (kJ/mol)	$A_{x\mathrm{B}}$ (kJ/mol)	$A_{x\mathrm{H}}$ (kJ/mol)	$\rho_{x\mathrm{Li}}$ (Å)	$\rho_{x\mathrm{B}}$ (Å)	$\rho_{x\mathrm{H}}$ (Å)
Li	0.8500	0.0	7793.7	7 375.3	0.4000	0.2853	0.3023
B	0.0	7793.7	0.0	0.0	0.2853	0.0000	0.2853
H	−0.1417	7375.3	0.0	209 905.0	0.3023	0.2853	0.2085

$k_{r,\mathrm{B-B}} = 125.0$ Å^{-2} kJ/mol, $r_{0,\mathrm{B-B}} = 1.79$ Å, $k_{r,\mathrm{B-H}} = 962.3$ Å^{-2} kJ/mol, $r_{0,\mathrm{B-H}} = 1.20$ Å, $k_{\theta,\mathrm{B-B-H}} = 83.7$ rad^{-2} kJ/mol, $\theta_{0,\mathrm{B-B-H}} = 120.0°$, $C_{\mathrm{H-H}} = 418.4$ Å^6 kJ/mol, and $C_{\mathrm{B-B,\ inter}} = 405.848$ Å^6 kJ/mol.

(β phase) [23]. The unit-cell parameters and atom coordinates were determined from single-crystal x-ray-diffraction data for the α phase reported by Her *et al.* [42]. Even though the α phase is the low-temperature phase and the β phase is the high-temperature phase, we performed MD simulation at the same temperature (600 K) for both phases. The starting structure for the β phase was taken to be the same as the α structure with cell parameter 10.02 Å. The core structures of the α and β phases are similar, with $B_{12}H_{12}{}^{2-}$ units located in the fcc position. However, B and H for the β phase had disordered lattice sites with an occupancy of 0.5 at high temperature, as identified in an experimental study [23]. In this simulation, the temperature was fixed using a Nosé-Hoover thermostat. Periodic boundary conditions were employed together with the Ewald summation technique for the convergence of long-range Coulombic interactions. A cutoff distance of 9.5 Å was used for the short- and long-range interactions. The run lengths were typically 5 ns long with a time step of 0.5 fs, including a 2-ns equilibrium preproduction run, and trajectory samples were stored during production run at regular intervals for further analysis. In addition, one long (25-ns) NVT-MD run was also performed for the α and β phases at 600 K to verify the stability of the system, and MD simulation was performed for a $3 \times 3 \times 3$ system for both phases to validate the system size dependency. Larger cutoff distances were also selected for the larger system and larger cell parameter cases. A few additional MD simulations were performed by varying the cell parameters from 9.9 to 10.2 Å with the same starting structure as α-phase at temperatures of 600–750 K with an interval of 50 K to understand the effect of the cell parameters on the cationic diffusion. NVT-MD simulations with fixed B and H were also performed to understand how the reorientational motion of the $B_{12}H_{12}^{2-}$ anion affects the cationic diffusion. To understand the effect of the degree of H freedom, NVT-MD simulation was also performed by employing a lower angular strength (nearly half of the current value, as mentioned in Table I), as discussed in Sec. III D.

FPMD simulation was performed to calculate the vibrational spectra, radial distribution functions (RDFs), and cation-hopping barrier to compare with the CMD results using the Vienna *Ab initio* Simulation Package (VASP) [43,44] of density-functional theory with plane-wave basis sets and projector-augmented-wave pseudopotentials [45,46] under periodic boundary conditions. We used van der Waals density functional (vdW-DF) correlation functionals [47,48] with the exchange functional optPBE to introduce van der Waals interaction [49–51]. An energy cutoff of 320 eV and $1 \times 1 \times 1$ k-point sampling were used. The initial structure of $Li_2B_{12}H_{12}$ consisted of $2 \times 2 \times 2$ unit cells (832 atoms in total) for the α and β phases at 600 K for 3 ps (1-ps equilibration and 2-ps sampling) with a time step of 0.4 fs.

III. RESULTS AND DISCUSSION

A. Validation of vibrational frequency and structure

To validate the classical potential model, the phonon vibrational modes were analyzed by calculating the vibrational density of states (VDOS). The VDOS was obtained from Fourier transform of the velocity autocorrelation function for both FPMD and CMD, and the results were compared (as shown in the Supplemental Material, Fig. S1 [52]). The peaks from CMD were close to those calculated from FPMD. Thus, our classical potential model, specifically the parameters involving B-B, B-H, and B-B-H, produced satisfactory FPMD-VDOS results.

The RDFs of the framework pairs, such as B-B, B-H, and H-H, and other pairs (Li-H and Li-B, etc.) were also calculated (as shown in the Supplemental Material, Figs. S2 and S3 [52]) at 600 K for the α and β phases from NVT-MD. The RDFs and $g(r)$s calculated from the x-ray-diffraction (XRD) structure of this material reported by Her *et al.* [42] are also shown in the same figure using vertical lines for structural comparison of the α phase. The peaks are consistent with the XRD and FPMD structure, and the bond lengths are almost the same for both phases. The coordination numbers are also close to those of the reported XRD structure, as shown in the Supplemental Material (SM), Fig. S4 [52]. Notably, the arm (faint first peak) of the H-H RDF appears because of the interanion $B_{12}H_{12}{}^{2-}$ H-H pair, which was also reproduced by the CMD. The same RDFs and coordination numbers in both phases were also observed for the larger ($3 \times 3 \times 3$) supercell. Therefore, our potential model supports the structure for both phases with high accuracy. Thus far, we can conclude that our potential model satisfactorily traces the energy minimum profile. However, the reliability of the potential also depends on how well it reproduces the transition states of ion hopping, which will be validated in the following sections.

B. Ionic motion

The cationic transport can be quantified by calculating the mean-square displacement (MSD) using the following

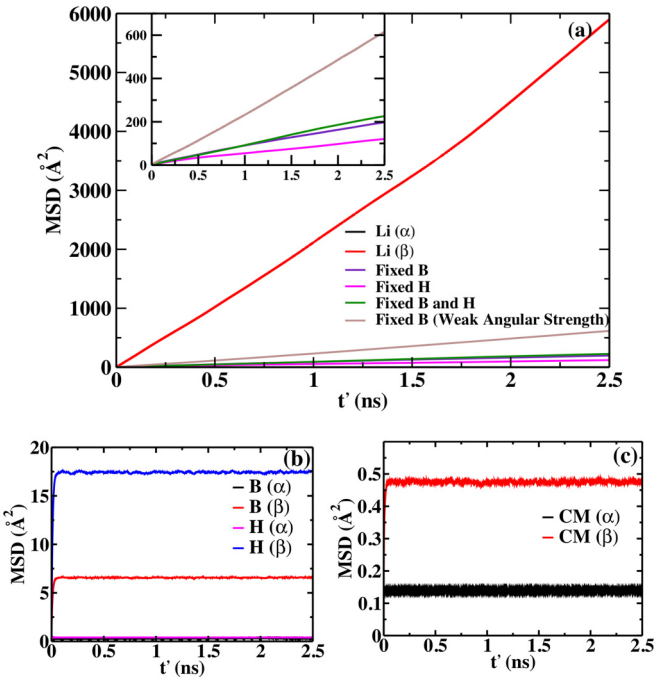

FIG. 2. (a) MSD of Li^+ ions at 600 K of α and β phases of $Li_2B_{12}H_{12}$ from NVT-MD simulation and for the cases of B and H fixed in the β phase and the weak angular strength case. The zoomed-in lower diffusion portion is shown in the inset. The MSD of Li (α) is not visible as it is close to zero. (b) MSD of B and H for both phases. (c) MSD of center of mass (CM) of borane units for both phases.

equation:

$$D = \lim_{t'\to\infty} \frac{1}{6Nt'} \left\langle \sum_{j=1}^{N} [\vec{r_j}(t+t') - \vec{r_j}(t)]^2 \right\rangle, \qquad (2)$$

where N is the number of mobile cations (Li^+) in the system, $\vec{r_j}(t+t')$ is the position vector of the jth ion after time interval t', and the angular brackets indicate the average over various time origins t. In the α phase, negligible Li^+-ion diffusion was observed, whereas in the β phase, significantly high Li^+-ion diffusivity was observed ($D = 0.39 \times 10^{-4}$ cm^2/s, with $D = 0.40 \times 10^{-4}$ cm^2/s reported by Varley *et al.* [53] from FPMD at 600 K), as shown in Fig. 2(a). MSDs of B and H were also calculated to understand the closo-borane dynamics, as shown in Fig. 2(b). The MSDs of B and H did not reveal translational motion in the α phase. However, the MSDs of B and H saturated rapidly (on the CMD timescale) to a constant value (6.5 Å^2 for B and 17.5 Å^2 for H), which are roughly half the square diameter of the closo-borane unit (distance of B or H to the center of mass of closo-borane).

The anions ($B_{12}H_{12}^{2-}$) are quasispherical in shape. However, the shape was more spherical than that of the anions (BH_4^-) and ($B_{10}H_{10}^{2-}$) of other hydride materials [54]. The MSD of the center of mass of the closo-borane was computed [Fig. 2(c)] to verify the stability of the structure, and it did not diffuse for both phases. The exact same trend and values were also observed for the larger ($3 \times 3 \times 3$) system. Therefore, the saturation of MSD of B or H in the β phase is solely due to the closo-borane reorientational motion.

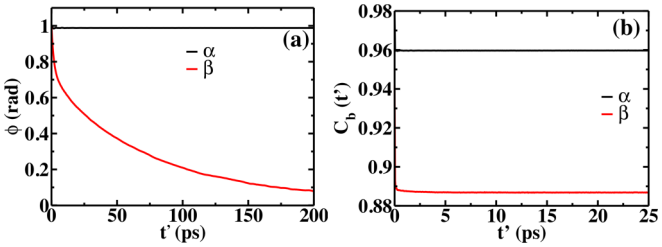

FIG. 3. (a) Angular autocorrelation function ϕ (t') of closo-borane anion from NVT-MD simulation at 600 K. The function in the β phase decays as $\sim e^{-\lambda t'}$, indicating a faster reorientational rate, whereas the α phase does not show decay on the CMD timescale. (b) Li-H bond fluctuation correlation, C_b (t') function for both phases are shown. The β phase exhibits a smaller saturation value, indicating higher bond fluctuation of the Li-H bond than for the α phase.

The angular autocorrelation function of the closo-borane units was computed to directly understand the rotational motion. A vector $\vec{r}(t)$ was connected from the center of mass of a borane unit to one edge (usually B or H; here, we consider only B atom) of the borane unit. The inner product was determined using the same vector after a time interval t' using the following equation:

$$\phi(t') = \langle \vec{r}(t) \cdot \vec{r}(t+t') \rangle. \qquad (3)$$

The function appears to decay exponentially with the decay rate, $\sim e^{-\lambda t'}$, within a short time range, as observed in Fig. 3(a). The $\phi(t')$ value in the α phase starts from unity and does not decay within the timescale of CMD. However, it drops to zero in the β phase within a few hundreds of picoseconds ($\lambda = 0.10 \times 10^9$ rad/s at 600 K, whereas 0.2×10^9 rad/s was reported by Varley *et al.* [53] at 800 K). Therefore, the result indicates no reorientational motion of the anions in the α phase, whereas significantly high anionic reorientational motion was observed in the β phase, resulting in variation of the H coordination around the Li site, which produces many disordered Li sites, as identified by XRD [23]. The variation of the coordination number of H also plays a major role in the cationic diffusion, which can be analyzed by calculating the dynamical fluctuation of the Li-H bond. To obtain a quantitative estimation, we define the bond-correlation function ζ (t') [55]. The following function is assigned: $\zeta(t') = 1$ if $r_{\mathrm{Li-H}} < 2.5$ Å (roughly first minimum distance of Li-H RDF), otherwise zero. The bond correlation was calculated as $C_b(t') = \langle \zeta(t)\zeta(t+t') \rangle$, averaging over all the cations for both phases. The value was higher for the α phase than for the β phase, which implies that the β phase exhibits more dynamical fluctuation [Fig. 3(b)] or variation of the H coordination number than the α phase. Although the values depend on the defined cutoff bond length, the trend remains the same.

C. Microscopic details

Understanding of the microscopic mechanism is important to understand the origin of fast ion conduction. Li-Li RDFs were calculated for both phases to understand the Li^+-ion

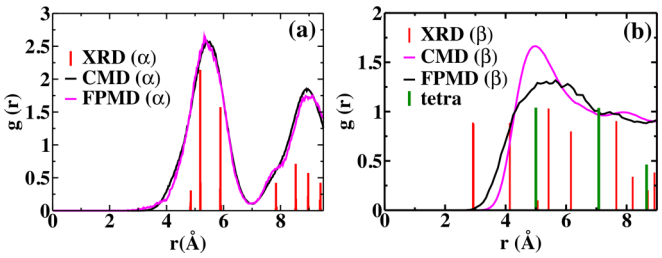

FIG. 4. Li-Li RDFs, $g(r)$s, for the (a) α phase and (b) β phase. The two-peak separation in (a) suggests the strong localization of the Li^+ ions, hindering the long-range motion. Two peaks are connected in (b), indicating the fast Li^+-ion diffusion. The red bars represent the RDFs from (a) 8*c* to 8*c* Li sites and (b) 24*d* to 24*d* Li sites. The green bar is the RDF from reported tetragonal sites to tetragonal sites [42].

diffusion pattern, as shown in Fig. 4. The first peak appeared roughly at a distance of 5.4 Å [Fig. 4(a)], which is close to the separation between the 8*c* Li site (near the circumcenter of the triangle formed by connecting three nearest-anion centers [42]) to the nearest 8*c* Li site (5.2 Å), as indicated by the red bars calculated from XRD. The solidlike nature of the Li-Li RDF [Fig. 4(a)] in the α phase indicates the strong localization of Li^+ ions at the Li sites (8*c*), resulting in negligible diffusion of Li^+ ions on classical MD timescales, as previously reflected in the MSD plot. For the β phase, the Li-Li RDF [Fig. 4(b)] exhibited a liquidlike nature. The first peak matches exactly with the tetragonal site to nearest-tetragonal site distances (5.0 Å), as indicated by the green bars. This result indicates that the Li^+ ions hop from the tetragonal site to the nearest tetragonal site through closely available disordered Li sites in favor of occupancy at the 8*c* and 24*d* Li sites, as identified by XRD [23] and previously reported FPMD [18]. However, all the sites are not simultaneously occupied as two Li^+ ions cannot come closer than 3 Å because of Li-Li repulsion, as observed from the MD simulation supported by the reported occupancy of 0.25 at 8*c* and 24*d* Li sites determined using XRD [23]. Therefore, smooth connectivity of the Li^+-ion channels between the nearest tetragonal Li sites through the disordered sites (8*c* and 24*d*) is expected. The hopping mechanism is also expected to be different in the two phases, as explained in the following text.

The self-van Hove correlation function, $G_s(r, t')$ [56] is important for understanding the ion-hopping mechanism. This function is defined as the probability of finding a particle at position r after time t':

$$G_s(r, t') = \frac{1}{N}\left\langle \sum_{i=1}^{N} \delta(\vec{r} - (\vec{r_i}(t') - \vec{r_i}(t + t')) \right\rangle. \quad (4)$$

The first-highest density near 1 Å of the α and β phases signifies the oscillatory behavior at the Li sites, and the next-highest density near distances of 6 Å for the α phase [Fig. 5(a)] and 5 Å for the β phase [Fig. 5(b)] results from the ion hopping to the neighboring sites. In the α phase, the hopping occurs from one interstitial 8*c* Li site to the nearest 8*c* Li sites as the distance 8*c* Li to 8*c* Li sites is approximately 5.2 Å, as observed in the Li-Li RDF in Fig. 4(a). The intensity of the color density at approximately 6 Å in Fig. 5(a) is very low, indicating less probable ion hopping, as reflected in the MSD plot in Fig. 2(a). In the β phase, the ion hopping occurs mainly from the tetragonal site to the nearest tetragonal site (as the tetragonal Li site to the nearest tetragonal Li site distance is approximately 5.0 Å) through the closely available disordered Li sites. However, all the closely available sites are not simultaneously occupied as the first peak appeared near 5.0 Å in the Li-Li RDF [Fig. 4(b)].

To determine the three-dimensional connectivity and Li^+-ion migration path, the coordinates of all the Li^+ ions in both phases were merged into a single unit cell, and the entire unit cell was divided into small cubic voxels to generate a density profile of the Li^+ ions. The Li^+-ion density plots reveal two different patterns for the α phase [Fig. 6(a)] and β phase [Fig. 6(b)], clearly reflecting two different hopping mechanisms, as previously discussed. The Li^+ density is confined to 8*c* Li sites in the α phase, whereas the isosurface plot of the β phase reveals distribution of the Li^+ density around the different Li sites. However, the maximum density was observed at the tetragonal Li sites and was well connected, resulting in high diffusivity. The Li^+ ions explore more accessible volume, which is possible because of the $B_{12}H_{12}^{2-}$ anionic reorientation. The quantitative occupancy at the different sites was determined by considering a sphere of radius 1.2 Å with the center at 8*c* Li, 24*d* Li, and tetragonal sites. Almost full occupancy at the 8*c* Li sites was observed in the α phase. For the β phase, occupancies of 0.1, 0.1, and

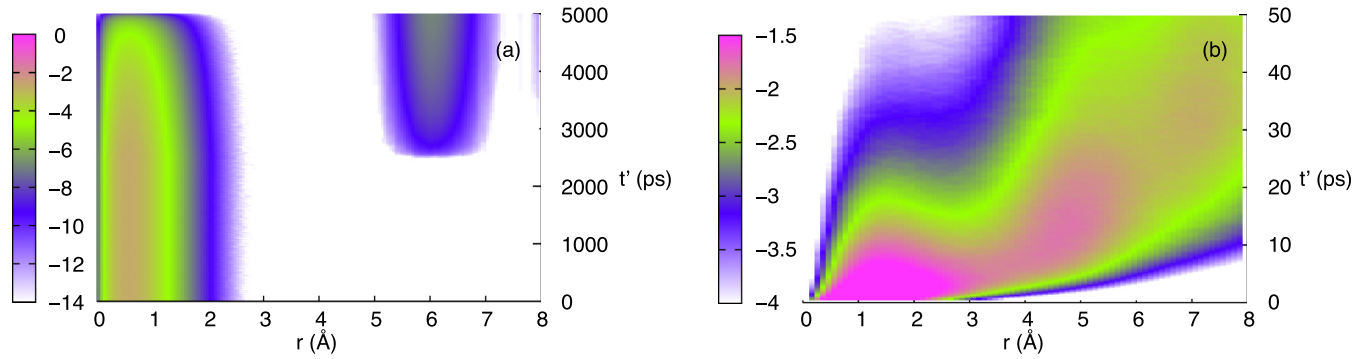

FIG. 5. Self-van Hove correlation function, $G_s(r, t')$, of Li^+ ions in the $Li_2B_{12}H_{12}$ system for the (a) α phase and (b) β phase from NVT-MD (the color bar is shown on a logarithmic scale).

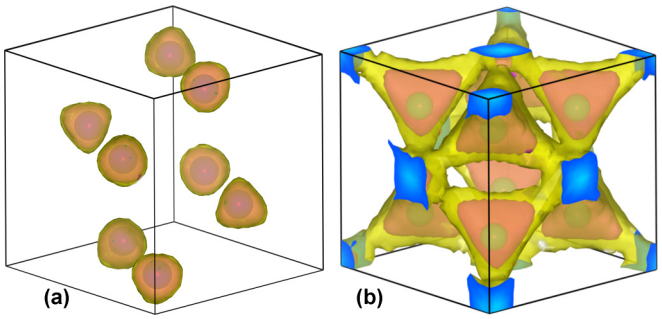

FIG. 6. Li^+-ion distribution isosurfaces in a single unit cell (the black line indicates the unit cell) for the (a) α phase and (b) β phase for isovalues of 4×10^{-5} Å^{-3} (yellow) and 8×10^{-5} Å^{-3} (magenta). The blue parts indicate the edges of the unit cell. The purple balls in the α phase represent 8c Li sites, and the green balls in the β phase represent tetragonal Li sites.

0.4 were observed at the 8c Li, 24d Li, and tetragonal sites, respectively, supporting entropy-driven diffusion [16,18,57]. The total occupancy was not unity, as ions were also detected in between the sites. The occupancy at the tetragonal sites was the highest, as qualitatively supported by the isosurface.

The probability density and free-energy barrier associated with the Li^+-ion hopping are key factors in determining the hopping path, which can be estimated by counting the number of Li^+ ions inside a cylinder of radius 2.0 Å (such that the full channel volume is covered) connecting two nearest maximum populated densities (from an 8c site to nearest 8c site for the α phase and from a tetragonal site to nearest tetragonal site for the β phase). This number is converted into probability density by dividing the total counts within the cylinder. The free energy (ΔF) is calculated using the equation $\Delta F = -k_B T \ln(p/p_{\max})$, where p is the probability density of Li^+-ion occupancy, $p_{\max}$ is the maximum probability density, k_B is the Boltzmann constant, and T is the system temperature. The probability density along the described direction is shown as the green line in Fig. 7(a), and the

TABLE II. Free-energy barrier (ΔF) for different cell parameters computed from Fig. 7(b).

a (Å)	ΔF (eV)
9.90	0.52
10.00	0.07
10.02 (β)	0.11
10.10	0.13
10.20	0.08

associated free-energy profile is presented in Fig. 7(b). The free-energy barrier of the Li^+-ion hopping in the β phase was significantly low (0.08 eV), as shown in Table II. The free-energy profile and barrier height were also computed from the FPMD simulation. The free-energy minima appeared at the tetragonal sites for the FPMD simulation, similar to the CMD simulation, as shown in the inset of Fig. 7(b). Therefore, the present potential model satisfactorily reproduces the transition free-energy barrier of cation hopping and density pattern.

The Li-Li RDFs, self-van Hove correlation functions, and probability density profiles revealed the Li^+ ions preferentially occupied the 8c site in the α phase and tetragonal sites in the β phase. Here, we attempt to investigate this behavior based on the H coordination number of different Li sites. The Li-H interaction is usually stronger than that of the other pairs. The Li site (8c Li) in the α phase had the highest H coordination numbers within the first minimum of the Li-H RDF [Fig. 8(a)] and the deepest potential minima (−2.58 eV) compared with the other Li sites (24d Li and tetragonal). However, the H coordination number of the tetragonal site was almost the same as those of other Li sites in the β phase [Fig. 8(b)]. The tetragonal sites were marginally energetically preferable (−2.50 eV) compared with the 8c (−2.48 eV) and 24d (−2.48 eV) sites. The potential energy values for the respective sites were calculated as follows. We considered a sphere with radius 1.2 Å and determined the number of

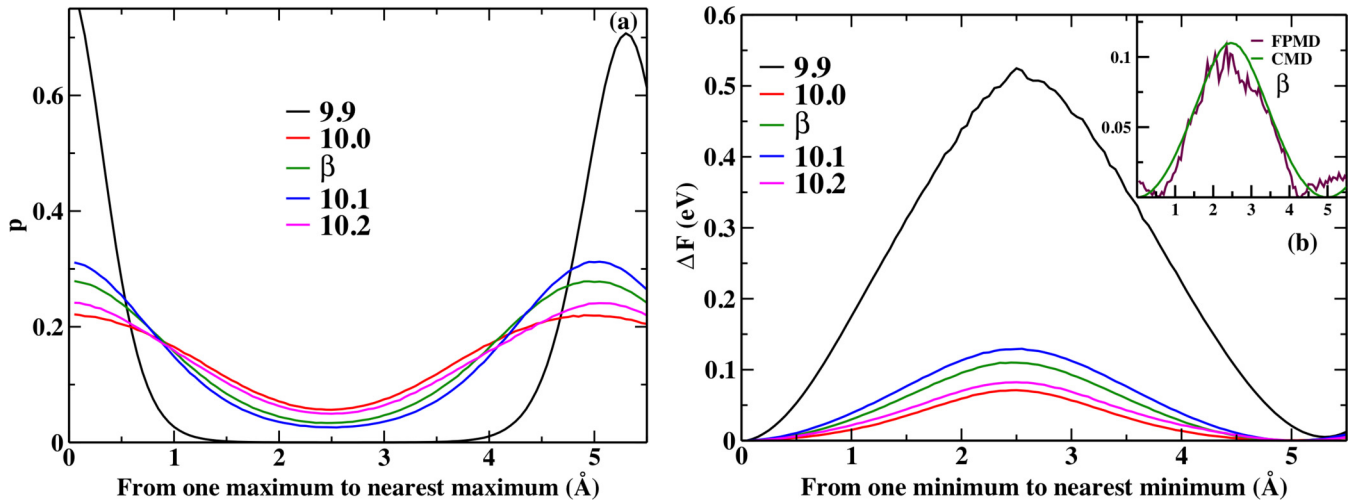

FIG. 7. (a) Occupancy probability density, p, along the path connecting two nearest density maxima as a function of distance for the β phase and for the system with different cell parameters and (b) corresponding free-energy barrier obtained using the equation $\Delta F = -k_B T \ln(p/p_{\max})$. The inset of Fig. (b) compares the FPMD and CMD free-energy profiles.

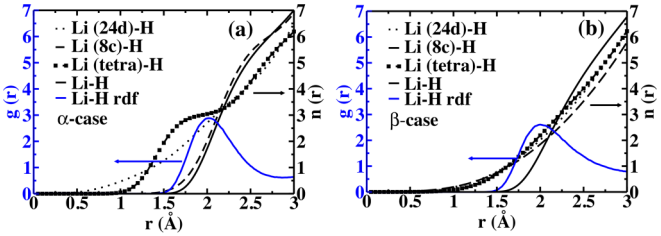

FIG. 8. RDF, $g(r)$, and coordination number, $n(r)$, of Li-H as a function of distance from the Li^+ ions or from the different Li sites for the (a) α phase and (b) β phase. The axis is indicated by respective colors, as directed by the arrows.

Li^+ ions as well as their potential energy within the sphere during the MD simulation. The average value was calculated by determining the total potential energy of all the Li^+ ions within the sphere divided by the total counts.

D. Influencing factors for cationic diffusion

The β phase has a higher cell volume than the α phase, which stimulates anions to reorient, generating the interstitial disordered Li sites, which might be the reason for percolated density pattern followed by low free-energy barrier. However, the core structure for both phases was the same, consisting of $B_{12}H_{12}^{2-}$ isolated icosahedral units arranged in fcc order. Therefore, it is important to understand the effect of the cell parameter on ionic diffusion. The cationic diffusion was investigated by systematically increasing the cell parameter.

The diffusivity and angular reorientational rate as a function of the lattice parameter are presented in Fig. 9(a) for lattice parameters of 9.8–10.2 Å. The diffusivity showed a sudden jump with increasing lattice parameter, and the maximum diffusivity was observed near 10.0 Å at 600 K (0.389×10^{-4} cm^2/s) and almost saturated thereafter, as previously reported for FPMD simulation [53]. For the lattice parameter of 10.0 Å (close to the lattice parameter of the β phase structure of 10.02 Å), significantly higher diffusivity is observed than that at 9.9 Å at 600 K. The angular reorientational rate also follows the same pattern as the diffusion coefficient pattern. Essentially, a larger cell parameter provides enough space for the anionic reorientation, which helps to generate numerous disordered Li sites. The sites are well connected for the system with a lattice parameter greater than 10 Å, and below this value, the Li^+-ion occupied part is almost isolated, which is consistent with the significantly low diffusivity.

The isosurface plots of Li density for different lattice parameters are presented in Fig. 10. The Li^+-ion density spreads and connects to the neighboring high-density sites in the system for lattice parameters greater than 10.0 Å. To obtain a quantitative understanding of the occupancy at the different Li sites, we counted the Li^+ ions by considering a sphere of radius 1.2 Å. The occupancy at the 8*c* Li site suddenly decreased with increasing cell parameter, as observed in Fig. 11. The occupancy of the system with a lattice parameter greater than 10 Å was fairly below unity at all of the sites, as reflected in Fig. 7(a). This result indicates that the Li^+ ions were more delocalized at various Li sites with a high level of entropy-driven diffusion of Li^+ ions observed, resulting in a low free-energy barrier, as observed in Fig. 7(b).

In addition to the cell parameter, temperature is another factor that stimulates anionic reorientational motion, resulting in high cationic diffusivity, as observed in the diffusivity and angular reorientational rate vs lattice parameters graphs for higher temperature (650, 700, and 750 K in Fig. 9(b) and in the Supplemental Material, Fig. S5 [52]). Similar diffusivity and reorientational patterns were observed, with marginally higher values of D or λ [comparison shown in Fig. 9(a)]. For higher temperature, the saturation occurred more rapidly, as also reported by Varley *et al.* [53]. For a particular temperature, the system needs a specific bottleneck cell parameter to allow anionic reorientation. As the temperature is fixed and the system already has enough volume to allow reorientation of

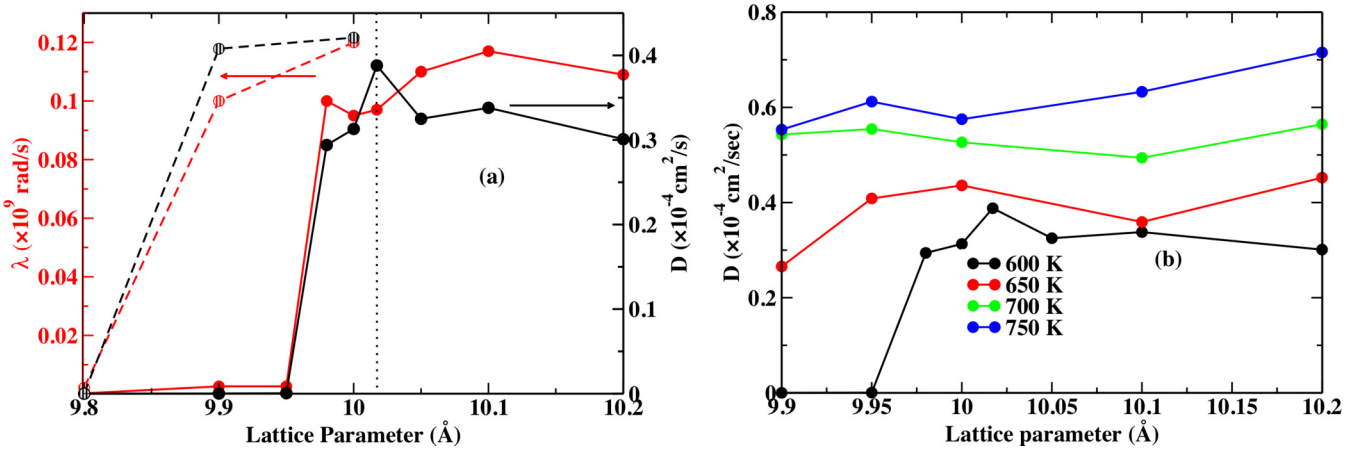

FIG. 9. (a) Diffusivity (D) as a function of lattice parameter (as indicated on the alternative y axis in black) and anionic reorientational rate (λ) as a function of cell parameter (as represented on the y axis in red). The initial structure was chosen from the α phase, and the lattice parameter is varied from 9.8 to 10.2 Å. The solid lines represent the results with the same B-B-H angular force parameter shown in Table I, and the dashed lines represent those with a weaker angular force parameter ($k_{B-B-H} = 41.84$ rad^{-2} kJ/mole). All the lines are drawn to guide the eye. The cell parameter of the β phase is marked by the dotted vertical lines. (b) Diffusivity (D) as a function of lattice parameter for the temperature range 600 to 750 K.

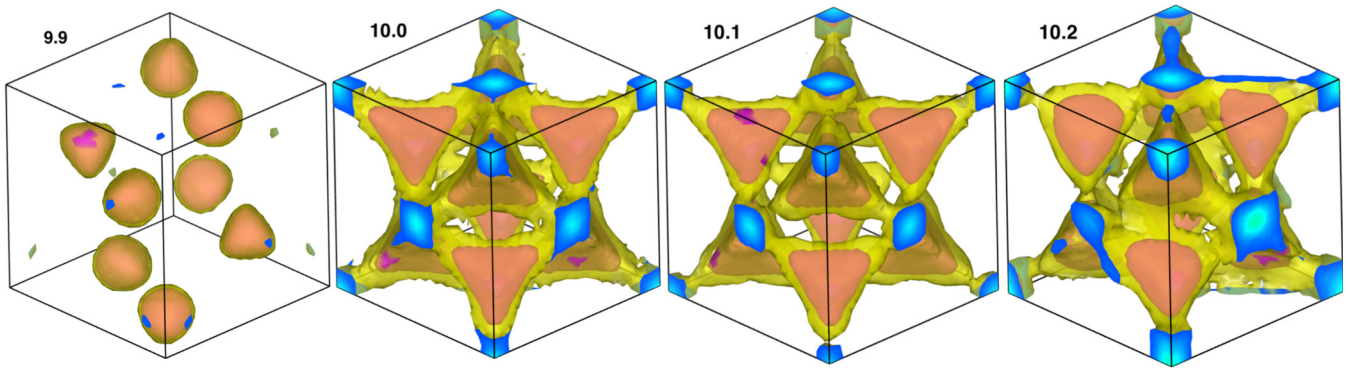

FIG. 10. Isosurface plots for the different lattice parameters (9.9, 10.0, 10.1, and 10.2 Å) for isovalues of 8×10^{-5} Å^{-3} (magenta) and 4×10^{-5} Å^{-3} (yellow). The blue color indicates the edges of the unit cell. The density pattern follows the α phase for the cell parameter of 9.9 Å and the β phase for the other cell parameters.

the anions, an even larger cell parameter does not produce any extra benefit for achieving an even faster reorientation rate, resulting in a marginal increase in the cationic diffusivity.

The anionic reorientational motion is understood to play a crucial role in the cationic diffusion. To understand this relationship more directly, the anion reorientation was stopped by freezing of the B or H atoms or both in the β phase, as compared with Varley *et al.* [53]. The β phase was selected as it exhibits high diffusivity. We also changed the force parameter in addition to freezing of B or H in the same system. All three cases resulted in roughly two orders of magnitude lower cationic diffusivity (0.740×10^{-6} cm^2/s) compared with that of the β phase [0.389×10^{-4} cm^2/s as shown in Fig. 2(a)] at 600 K as no reorientational motion of anions was allowed. Therefore, Li^+ ions were no longer assisted by the anions to enable exploration of the accessible volume, hindering the long-range motion of the Li^+ ions. However, the diffusivity was higher than the α phase, as few sites in addition to 8*c* among all the disordered sites were found because of the larger cell volume. Thus, anionic reorientational motion plays

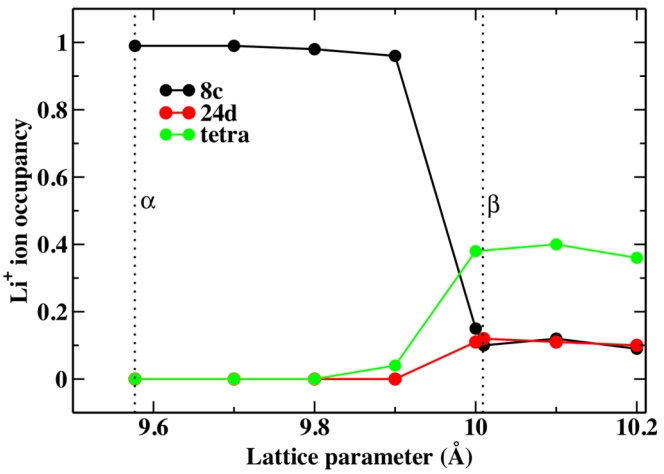

FIG. 11. Occupancy inside a sphere of radius 1.2 Å at respective Li sites for different cell parameter cases. The initial structure was chosen from the α phase, and the lattice parameter is varied from 9.58 to 10.20 Å. The XRD cell parameters of the α and β phases are marked by the dotted vertical lines.

both the role of generating disorder Li-sites and guiding Li^+ ions to explore all the available sites following the possible mechanism, as suggested for $Ag_2B_{12}H_{12}$ system [58].

For the α phase, where the low cell volume does not allow reorientation of the anion, the access of Li^+ ions to all of the accessible volume is restricted, resulting in negligible Li^+-ionic diffusion. In this context, we expected that H flexibility plays an important role in the cationic diffusion. To understand the role of H flexibility, we set a weak angular strength ($k_{B-B-H} = 41.84$ rad^{-2} kJ/mol, which is almost two times weaker than that of the current system), and the system exhibited significantly higher reorientational motion and fairly high Li^+-ion conductivity beyond a lattice parameter of 9.9 Å (0.41×10^{-4} cm^2/s) compared with the usual angular strength case (0.13×10^{-7} cm^2/s), as shown in Fig. 9(a). The density pattern of the Li^+ ions and the occupancies at the different sites were also similar as those for the other usual high-conducting cases. Essentially, the weaker angular harmonic strength makes the anions softer, which enables the anionic reorientation inside a smaller unit cell. However, the significant cationic diffusion, where the reorientational rate already reaches saturation (larger unit-cell case), is not affected.

The H flexibility was also tested in the fixed B and H cases, where almost two times higher the diffusivity was observed, as shown in the inset of Fig. 2(a). Even though this study appears to be purely theoretical, it draws attention to possible substitution or other chemical treatments which might make the anion softer to enable the low-temperature phase (even for small cell parameter) to exhibit high ionic conductivity.

IV. CONCLUSION

In conclusion, an interatomic potential model was developed for the $Li_2B_{12}H_{12}$ system for classical MD simulation that reproduces the results (vibrational spectra, structure, diffusivity, and transition state of ion-hopping barrier) obtained or reported using first-principles MD and experiments. Negligible diffusion was observed for the low-temperature α phase. In contrast, high diffusivity was observed for the high-temperature β phase, consistent with previous reports in the literature. High reorientational motion was indirectly observed by calculating the MSD of B and H and the center

of mass of the anions and was directly supported by the angular autocorrelation function. The $B_{12}H_{12}^{2-}$ reorientation is understood to play a significant role in the Li^+-ion diffusion as higher reorientation of $B_{12}H_{12}^{2-}$ was observed in the β phase. Essentially, reorientational motion yields disordered Li sites in the β phase, as supported by the 3D isosurface of the density, counting at different Li sites, and self-van Hove correlation functions. Furthermore, insight into the fast diffusion was obtained by modifying the MD controlling parameters, some of which are impossible to modify in a real system or using first-principles MD. Larger cell parameters allowed anions to reorient, resulting in an extraordinary increase of Li^+ diffusion with increasing cell parameter followed by saturation. The same trend was observed for the temperature change over the mentioned range with faster saturation. The reorientational rate also followed the same pattern, clearly indicating that cationic diffusion is strongly coupled to the reorientational rate. Therefore, controlling the reorientational rate is important to maximize ionic conduction. A deeper study is needed to understand how different modes (rotational or librational) of anion and different anionic valency ($CB_9H_{10}^-$ or $CB_{11}H_{12}^-$), size, and shape (such as ellipsoidal $B_{10}H_{10}$) influence ionic conduction. In addition, we also investigated the cationic motion by freezing of B or H and changing the hydrogen angular force parameter. The results indicated that the hydrogen dynamics plays an important role in the cation dynamics, which was further understood when H was given more freedom by weakening the angular strength. Essentially, the lower angular strength makes the anions softer, which allows anionic reorientation inside a relatively smaller cell, with the trends indicating possibility of achieving significantly high cationic diffusivity even at lower temperature. The phenomena might be achievable experimentally by substitution or through other means. Our findings help us understand the factors that explicitly influence cationic diffusion.

This study revealed the microscopic mechanism and factors influencing fast ion transport in this system. The current potential model may also be transferable to other materials of this promising class of solids and will help to investigate the substitutional effect on fast ion transport. Our findings will help accelerate future computational studies and open up the possibility of several virtual experiments for improving our current theoretical understanding.

ACKNOWLEDGMENTS

The computations were performed at the computational facilities at the Center for Computational Materials Science, Institute for Materials Research, Tohoku University, Japan. We acknowledge JSPS KAKENHI Grant No. JP18H05513 and Advanced Target Project of WPI–AIMR, Tohoku University for research funding. K.S. acknowledges Professor P. Padma Kumar for useful discussions. We would also like to thank Tiffany Jain, M.S., from Edanz Group (www.edanzediting.com/ac) for editing a draft of this manuscript.

[1] A. Manthiram, X. Yu, and S. Wang, Nat. Rev. Mater. **2**, 16103 (2017).
[2] D. Lin, Y. Liu, and Y. Cui, Nat. Nanotechnol. **12**, 194 (2017).
[3] J. Janek and W. G. Zeier, Nat. Energy **1**, 16141 (2016).
[4] J.-M. Tarascon and M. Armand, Nature (London) **414**, 359 (2001).
[5] S. Adams and R. Prasada Rao, J. Mater. Chem. **22**, 7687 (2012).
[6] G. K. Phani Dathar, J. Balachandran, P. R. C. Kent, A. J. Rondinone, and P. Ganesh, J. Mater. Chem. A **5**, 1153 (2017).
[7] N. Kamaya, K. Homma, Y. Yamakawa, M. Hirayama, R. Kanno, M. Yonemura, T. Kamiyama, Y. Kato, S. Hama, K. Kawamoto, and A. Mitsui, Nat. Mater. **10**, 682 (2011).
[8] V. Thangadurai, S. Narayanan, and D. Pinzaru, Chem. Soc. Rev. **43**, 4714 (2014).
[9] R. Jalem, M. J. D. Rushton, W. Manalastas, M. Nakayama, T. Kasuga, J. A. Kilner, and R. W. Grimes, Chem. Mater. **27**, 2821 (2015).
[10] H.-P. Hong, Mater. Res. Bull. **11**, 173 (1976).
[11] J. B. Goodenough, H. Y. P. Hong, and J. A. Kafalas, Mater. Res. Bull. **11**, 203 (1976).
[12] H. I. Schlesinger, H. C. Brown, B. Abraham, A. C. Bond, N. Davidson, A. E. Finholt, J. R. Gilbreath, H. Hoekstra, L. Horvitz, E. K. Hyde, J. J. Katz, J. Knight, R. A. Lad, D. L. Mayfield, L. Rapp, D. M. Ritter, A. M. Schwartz, I. Sheft, L. D. Tuck, and A. O. Walker, J. Am. Chem. Soc. **75**, 186 (1953).
[13] T. J. Udovic, M. Matsuo, A. Unemoto, N. Verdal, V. Stavila, A. V. Skripov, J. J. Rush, H. Takamura, and S. I. Orimo, Chem. Commun. **50**, 3750 (2014).
[14] A. Unemoto, M. Matsuo, and S. I. Orimo, Adv. Funct. Mater. **24**, 2267 (2014).
[15] W. S. Tang, M. Matsuo, H. Wu, V. Stavila, W. Zhou, A. A. Talin, A. V. Soloninin, R. V. Skoryunov, O. A. Babanova, A. V. Skripov, A. Unemoto, S. I. Orimo, and T. J. Udovic, Adv. Energy Mater. **6**, 1502237 (2016).
[16] W. S. Tang, M. Matsuo, H. Wu, V. Stavila, A. Unemoto, S. Orimo, and T. J. Udovic, Energy Storage Mater. **4**, 79 (2016).
[17] W. S. Tang, A. Unemoto, W. Zhou, V. Stavila, M. Matsuo, H. Wu, S. Orimo, and T. J. Udovic, Energy Environ. Sci. **8**, 3637 (2015).
[18] K. E. Kweon, J. B. Varley, P. Shea, N. Adelstein, P. Mehta, T. W. Heo, T. J. Udovic, V. Stavila, and B. C. Wood, Chem. Mater. **29**, 9142 (2017).
[19] S. Kim, N. Toyama, H. Oguchi, T. Sato, S. Takagi, T. Ikeshoji, and S. I. Orimo, Chem. Mater. **30**, 386 (2018).
[20] S. Kim, H. Oguchi, N. Toyama, T. Sato, S. Takagi, T. Otomo, D. Arunkumar, N. Kuwata, J. Kawamura, and S. Orimo, Nat. Commun. **10**, 1081 (2019).
[21] Z. Łodziana and T. Vegge, Phys. Rev. Lett. **93**, 145501 (2004).
[22] D. Blanchard, A. Nale, D. Sveinbjörnsson, T. M. Eggenhuisen, M. H. W. Verkuijlen, Suwarno, T. Vegge, A. P. M. Kentgens, and P. E. De Jongh, Adv. Funct. Mater. **25**, 184 (2015).
[23] M. Paskevicius, M. P. Pitt, D. H. Brown, D. A. Sheppard, S. Chumphongphan, and C. E. Buckley, Phys. Chem. Chem. Phys. **15**, 15825 (2013).

[24] R. Mohtadi and S. I. Orimo, Nat. Rev. Mater. **2**, 16091 (2016).
[25] Z. Lu and F. Ciucci, J. Mater. Chem. A **4**, 17740 (2016).
[26] P. Padma Kumar and S. Yashonath, J. Phys. Chem. B **106**, 7081 (2002).
[27] M. P. Allen and D. J. Tildesley, *Computer Simulation of Liquids* (Oxford Science, Oxford, 2008).
[28] D. Frenkel and B. Smit, *Understanding Molecular Simulation: From Algorithms to Applications*, Computational Science Series (Elsevier, Amsterdam, 2002), Vol. 1.
[29] K. I. Nomura, Y. Yokoyama, and M. Kobayashi, Solid State Ionics **154–155**, 285 (2002).
[30] M. A. Zendejas and J. O. Thomas, Phys. Scr. **T33**, 235 (1990).
[31] K. Sau and P. P. Kumar, J. Phys. Chem. C **119**, 1651 (2015).
[32] K. Sau and P. P. Kumar, J. Phys. Chem. C **119**, 18030 (2015).
[33] K. Sau, AIP Conf. Proc. **1728**, 020119 (2016).
[34] K. Sau, Ionics **22**, 2379 (2016).
[35] S. H. Jung, F. Federici Canova, and K. Akagi, J. Phys. Chem. A **120**, 364 (2016).
[36] M. Parrinello, A. Rahman, and P. Vashishta, Phys. Rev. Lett. **50**, 1073 (1983).
[37] P. Boolchand and W. J. Bresser, Nature (London) **410**, 1070 (2001).
[38] A. Ivanov-Schitz, Solid State Ionics **159**, 63 (2003).
[39] P. Vashishta and A. Rahman, Phys. Rev. Lett. **40**, 1337 (1978).
[40] S. Roy and P. Padma Kumar, Phys. Chem. Chem. Phys. **15**, 4965 (2013).
[41] S. Plimpton, J. Comput. Phys. **117**, 1 (1995).
[42] J. H. Her, M. Yousufuddin, W. Zhou, S. S. Jalisatgi, J. G. Kulleck, J. A. Zan, S. J. Hwang, R. C. Bowman, and T. J. Udovic, Inorg. Chem. **47**, 9757 (2008).
[43] G. Kresse and J. Hafner, Phys. Rev. B **47**, 558 (1993).
[44] A. R. Miedema, J. Less Common Met. **32**, 117 (1973).
[45] P. E. Blöchl, Phys. Rev. B **50**, 17953 (1994).
[46] G. Kresse and D. Joubert, Phys. Rev. B **59**, 1758 (1999).
[47] M. Dion, H. Rydberg, E. Schröder, D. C. Langreth, and B. I. Lundqvist, Phys. Rev. Lett. **92**, 246401 (2004).
[48] G. Román-Pérez and J. M. Soler, Phys. Rev. Lett. **103**, 096102 (2009).
[49] J. Klimeš, D. R. Bowler, and A. Michaelides, J. Phys.: Condens. Matter **22**, 022201 (2010).
[50] J. Klimeš, D. R. Bowler, and A. Michaelides, Phys. Rev. B **83**, 195131 (2011).
[51] J. P. Perdew, K. Burke, and M. Ernzerhof, Phys. Rev. Lett. **77**, 3865 (1996).
[52] See Supplemental Material at http://link.aps.org/supplemental/10.1103/PhysRevMaterials.3.075402 for power spectra, structural, and dynamical properties.
[53] J. B. Varley, K. Kweon, P. Mehta, P. Shea, T. W. Heo, T. J. Udovic, V. Stavila, and B. C. Wood, ACS Energy Lett. **2**, 250 (2017).
[54] T. J. Udovic, M. Matsuo, W. S. Tang, H. Wu, V. Stavila, A. V. Soloninin, R. V. Skoryunov, O. A. Babanova, A. V. Skripov, J. J. Rush, A. Unemoto, H. Takamura, and S. Orimo, Adv. Mater. **26**, 7622 (2014).
[55] N. Adelstein and B. C. Wood, Chem. Mater. **28**, 7218 (2016).
[56] P. Hopkins, A. Fortini, A. J. Archer, and M. Schmidt, J. Chem. Phys. **133**, 224505 (2010).
[57] W. S. Tang, T. J. Udovic, and V. Stavila, J. Alloys Compd. **645**, S200 (2015).
[58] M. Paskevicius, B. R. S. Hansen, M. Jørgensen, B. Richter, and T. R. Jensen, Nat. Commun. **8**, 15136 (2017).